Supporting Information

Highly Crystallized Prussian Blue with Enhanced Kinetics for Highly Efficient Sodium Storage

Mingsheng Qin[†], Wenhao Ren[‡], Ruixuan Jiang[†], Qi Li[†§], Xuhui Yao[†], Shiqi Wang[†], Ya You[†*] and Liqiang Mai[†§*]*

§ Foshan Xianhu Laboratory of the Advanced Energy Science and Technology Guangdong Laboratory

Xianhu Hydrogen Valley,

Foshan 528200, Guangdong, China.

† State Key Laboratory of Advanced Technology for Materials Synthesis and Processing

Wuhan University of Technology

Wuhan 430070, Hubei, P. R. China.

* E-mail: qi.li@whut.edu.cn, youya@whut.edu.cn, mlq518@whut.edu.cn

‡ School of Chemistry, Faculty of Science

The University of New South Wales,

Sydney, New South Wales 2052, Australia.

Experimental Section

Material synthesis

Synthesis of H-PB: Prussian blue with high crystallinity (H-PB) was prepared through a facile hydrothermal process. Firstly, 2 mmol $Na_4Fe(CN)_6$, 4 mmol sodium citrate and 10 g NaCl were dissolved in a mixed solution containing 60 ml H_2O and 5 ml HCl (37%). After vigorous stirring for 10 min, a clear yellow solution was obtained. Then, the mixture was transferred into a 100 ml Teflon-lined autoclave and kept at 70 °C oven for 24 h. After cooled down to room temperature naturally, the blue precipitate was collected and washed with distilled water and ethanol for several times. Finally, the obtained sample was dried at 100 °C in a vacuum oven overnight to remove the absorbed water. Different contents of sodium citrate were added to modulate the crystallinity.

Synthesis of L-PB: Prussian blue with low crystallinity (L-PB) was synthesized via a conventional coprecipitation route as reported in previous work.[1] Firstly, 2 mmol $FeCl_3$ was dissolved in 50 ml distilled water and stirred for 10 min to prepare solution A. Another solution B was obtained by dissolving 1.5 mmol $Na_4Fe(CN)_6$ in 50 ml water. Then, solution A was quickly poured into solution B and continued stirring at 70 ºC for 4 h. After washing and drying as the same as H-PB, the deep blue sample named L-PB was obtained.

Synthesis of hard carbon: Hard carbon was obtained through a biomass method.[2] Firstly, the white internal capsule in shaddock peel was carefully washed with distilled water and ethanol several times to remove impurities. After cutting into proper size and drying in 140 ºC oven for 2 days, the sample was carbonized at 1200 ºC for 3 h in floating Ar atmosphere. Then, the obtained black powder was grinded and deliberately stirred in a 3 M HCl (37%) solution overnight to remove the remaining impurities. Finally, the hard carbon can be obtained after washing with water and drying in the oven.

Material characterization: X-ray diffraction patterns (XRD) of these samples were collected via the Bruker D8 Discover X-ray diffractometer (Cu Kα, λ = 1.5418 Å). The morphological characterizations were investigated by JEOL-7100F at voltage of 15 kV. Transmission electron microscopy (TEM), and high-resolution TEM (HRTEM) images were collected by using the JEM-2100F microscope. Brunauer-Emmett-Teller (BET) surface area was tested by Tristar II 3020. Renishaw INVIA micro-Raman spectroscopy system was employed to investigate the Raman spectra. X-ray photoelectron spectroscopy (XPS) analyses were done on VG Multilab 2000.4. TGA was performed using a Netzsch STA 449 F5 simultaneous analyzer from room temperature to 500 ℃ in N_2 atmosphere. The Mössbauer measurements were performed via Germany, Wissel MS-500 in transmission geometry. The results were fitted by the Recoil using Lorentzian Multiplet Analysis. The Rietveld refinements were performed on software GSAS.[3]

Electrochemical measurements: The half cell performance was measured on battery testing system (LAND CT2001A) by assembling CR2016-type coin cells with Na metal foil and the as synthesized materials. The cathode of Prussian blue was composed of 60% active materials, 30% Ketjen black, and 10% poly(tetrauoroethylene) (PTFE) binder. Typically, the mass loading of active materials in cathode was about 2 mg cm^{-2}. The solution of $NaClO_4$ in ethylene carbon (EC), dimethyl carbonate (DMC) (1:1 w/w) and 10% fluoroethylene carbonate (FEC) was employed as the electrolyte. A glass microfiber filter (Grade GF/A) was used as the separator. Before testing, the coin cell was aged for 10 h to reach a normal state. The electrochemical measurements including galvanostatic charge/discharge, rate performance and GITT were performed on LAND CT2001A. Cycling voltammetry (CV) and electrochemical impedance (EIS) were collected by electrochemical workstation of Autolab PGSTAT302N). For the Na-ion full batteries, the homemade hard carbon was employed as anode. The slurry including 70% hard carbon, 20% acetylene black and 10% carboxyl methyl cellulose (CMC) binder was cast

onto Cu foil and dried at 60 ℃ overnight to get the anode. Before full cell assembly, the anode was cycled for 10 cycles to get a stable SEI and compensate the depletion of Na^+. The cathode was discharged to 2 V. The specific capacity of full cell was calculated based on the cathode.

In-situ measurements: The special battery model was used for in situ measurements. In situ XRD signals were collected using the VANTEC-500 detector in a still mode, and each diffraction pattern was collected for 90 s. During measurements, the X-rays penetrate the beryllium window on the battery model and detect the signal of structural evolution. In situ Raman spectroscopy was collected in Renishaw INVIA micro-Raman spectroscopy system, and Raman signal was recorded with a time interval of 100 s. The battery for in situ measurements was the same as half cell except for using the special battery model, and the electrode was cycled with 2 C (240 mA g^{-1}) during measurements.
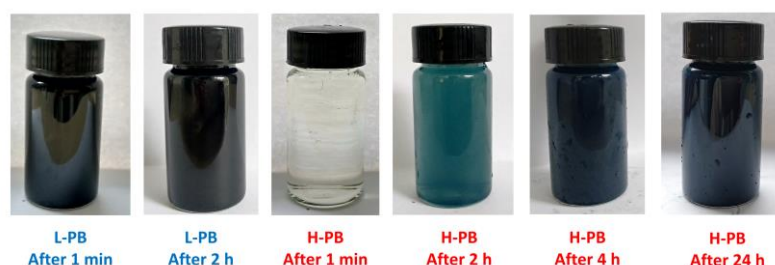

Figure S1. The pictures of aqueous solution for L-PB and H-PB collected at different reaction time.

A dark blue precipitation can be obtained immediately for the L-PB due to the rapid coordination of Fe^{3+} and $[Fe(CN)_6]^{4-}$. The reaction is too fast to guarantee the perfect lattice, resulting in low crystallinity, abundant defects and even accumulation of crystal water. However, the coordination rate is much slower for H-PB, leading to the formation of highly crystallized Prussian blue.
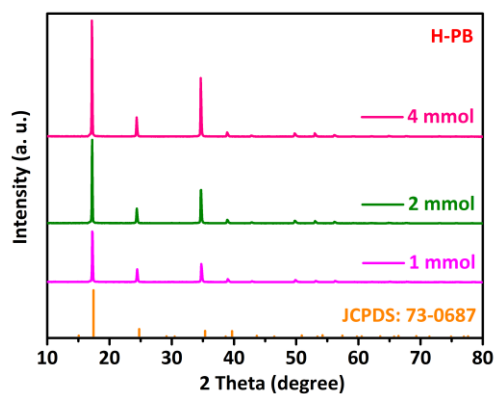
Figure S2. XRD patterns of the as synthesized Prussian blue collected with different contents of sodium citrate.
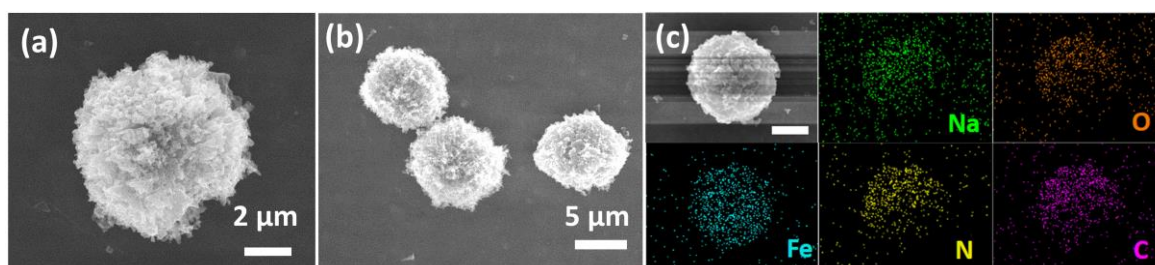

Figure S3. a, b) SEM images and c) EDS mappings for H-PB.
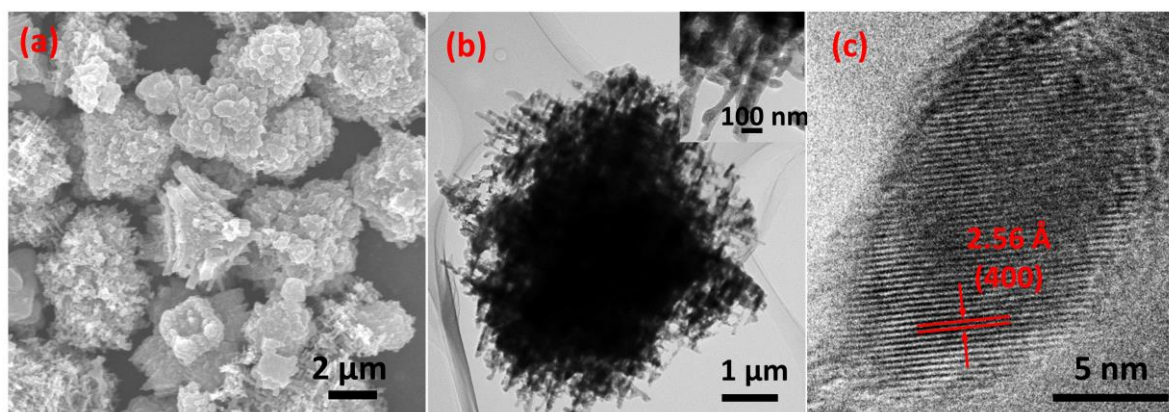

Figure S4. a) SEM image, b) TEM image and c) HRTEM image of H-PB. The lattice fringe with spacing value of 2.56 Å is coincide with the (400) plane of $Fe_4[Fe(CN)_6]_3$.
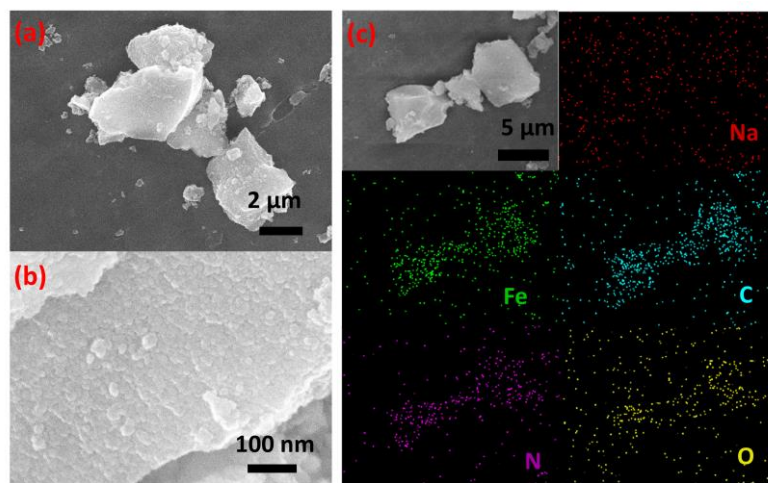
Figure S5. Morphologic characterizations of L-PB. a, b) SEM images for L-PB. c) EDS mappings of L-PB. The weak signal for Na indicates that few Na$^+$ exist in the bulk phase due to the rapid coprecipitation process.
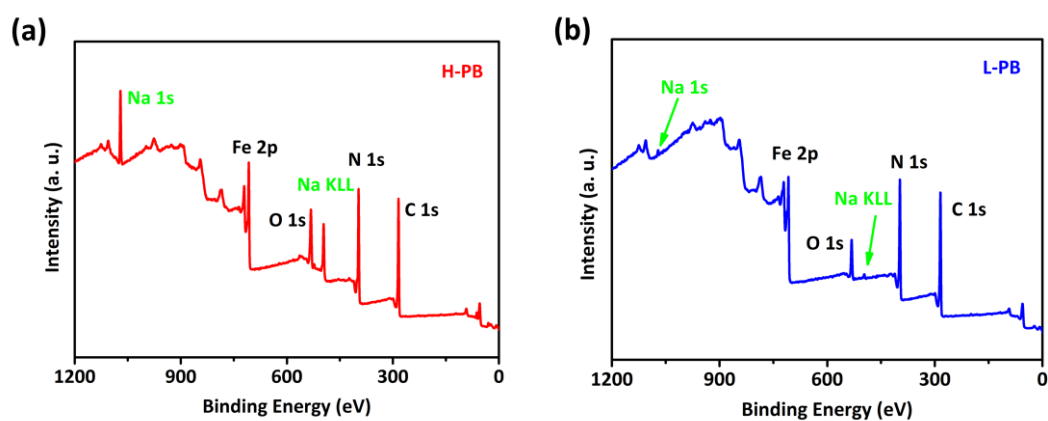

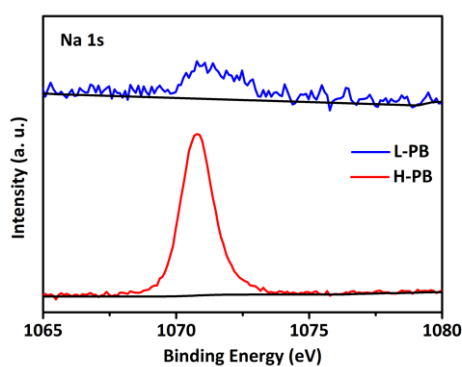**Figure S6.** The XPS results of a) H-PB and b) L-PB.

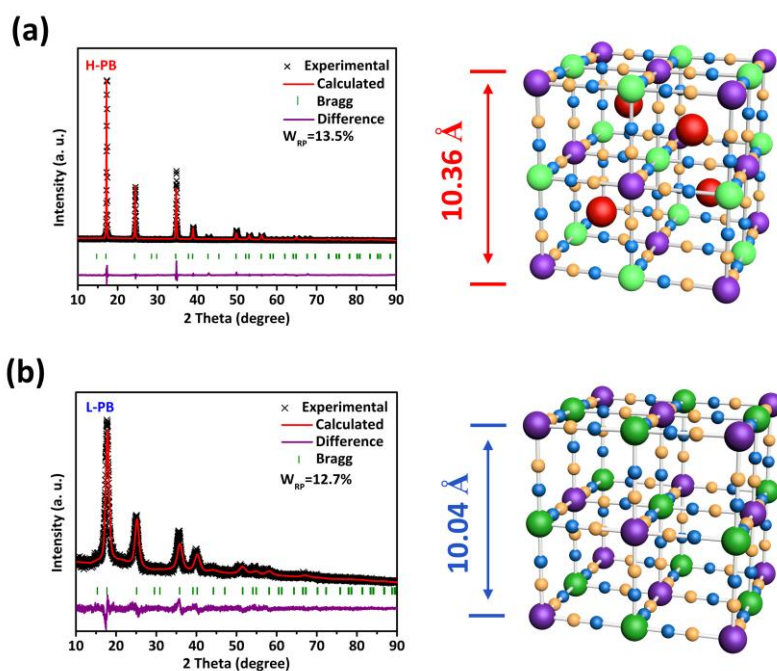**Figure S7.** The XPS results of Na 1s.

Figure S8. Rietveld refinements for a) H-PB and b) L-PB, and corresponding general view for the typical face-centered-cubic structure. (Red ball: Na; Brown ball: C; Blue ball: N; Purple ball: LS-Fe; Green ball: HS-Fe).
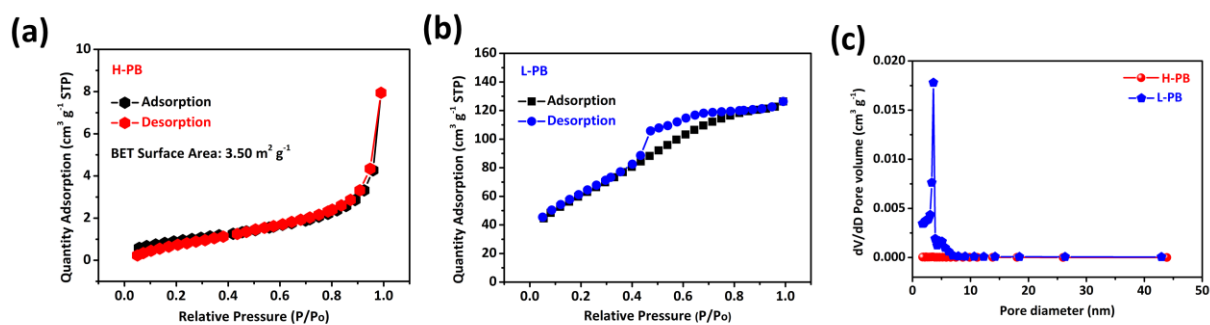

Figure S9. a,b) Nitrogen adsorption-desorption isotherms for H-PB and L-PB. The calculated surface area of L-PB is 221.3 m^2 g^{-1}. c) The pore size distributions for H-PB and L-PB.
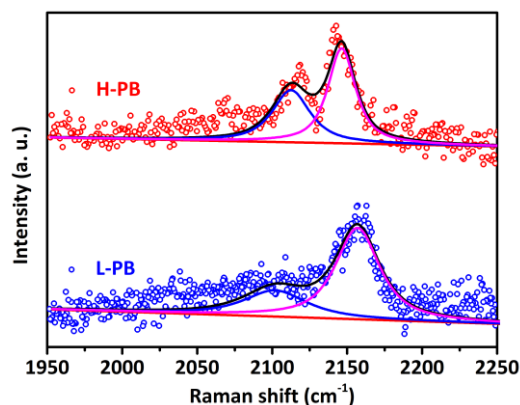
Figure S10. Raman spectra of H-PB and L-PB. The higher intensity of peak located at 2110 cm^{-1} indicates the lower average valence in H-PB.
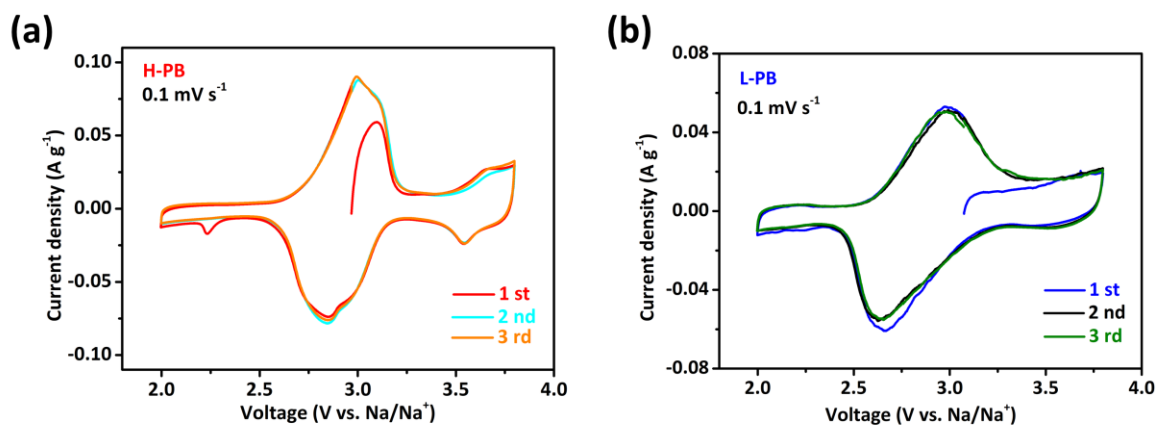

Figure S11. The first three CV curves at 0.1 mV s^{-1} for a) H-PB and b) L-PB. The open-circuit voltages (OCV) are 2.95 and 3.05 V for H-PB and L-PB, respectively, manifesting a lower average valence state of Fe in H-PB. Notably, a strong peak current is observed for H-PB during the first anodic process, indicating the higher extraction of Na^{+}. In the subsequent cycles, the CV curves of H-PB show small peak separations and good overlapping, arising from the superior kinetics and good reversibility. Moreover, a small cathodic peak located at 2.2 V can be observed for H-PB only during the first cycle, which is ascribed to the electrochemical adsorption of Na^{+}, as explained in Figure S12.
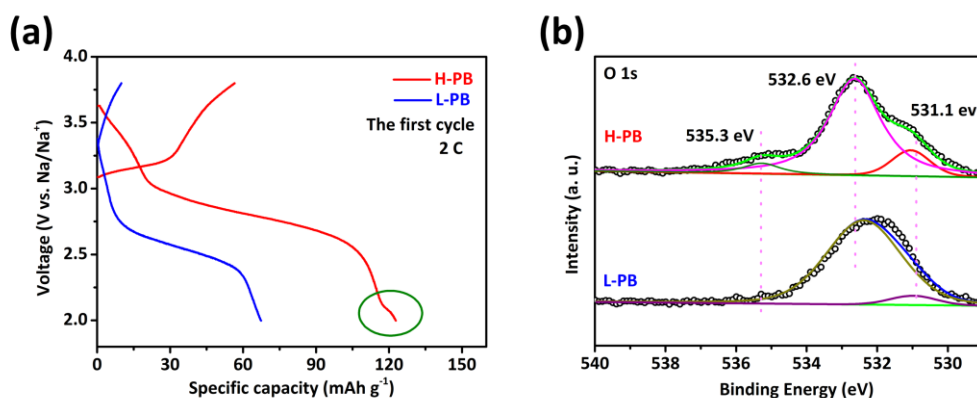
Figure S12. a) The first charge and discharge curves, b) XPS results of O 1s for H-PB and L-PB.

Apparently, a small discharge plateau is presented in H-PB at 2.2 V. The signal of O 1s on the surface was revealed to explain this abnormal phenomenon. All curves were calibrated by setting the C 1s BE region at 284.5 eV, and the main peak situated at 532.6 eV is ascribed to the physic/chemi-sorbed water and the oxygen ions in low coordination.[4] However, the surface of H-PB is slightly hydroxylated (531.1 eV) and carboxylated (535.3 eV) during the hydrothermal process with sodium citrate. The partially functionalized surface of H-PB might leads to the electrochemical adsorption of Na^+ at 2.2 V during the first cycling.[5-6]
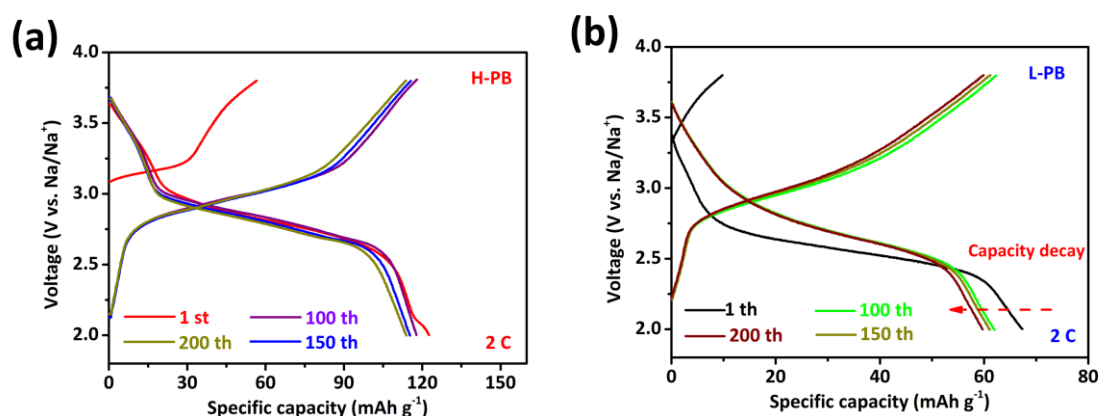

Figure S13. The charge and discharge curves of a) H-PB and b) L-PB at a current density of 2 C. The small voltage hysteresis of 120 mV is exhibited in H-PB, while a hysteresis of 504 mV is observed in L-PB. The much inhibited voltage hysteresis demonstrates the favor reaction

kinetics in H-PB. The small tail at the end of discharge is attributed to electrochemical adsorption from the hydroxylated surface of H-PB as discussed in the Figure S12. This electrochemical adsorption is irreversible and disappears in the following cycling.
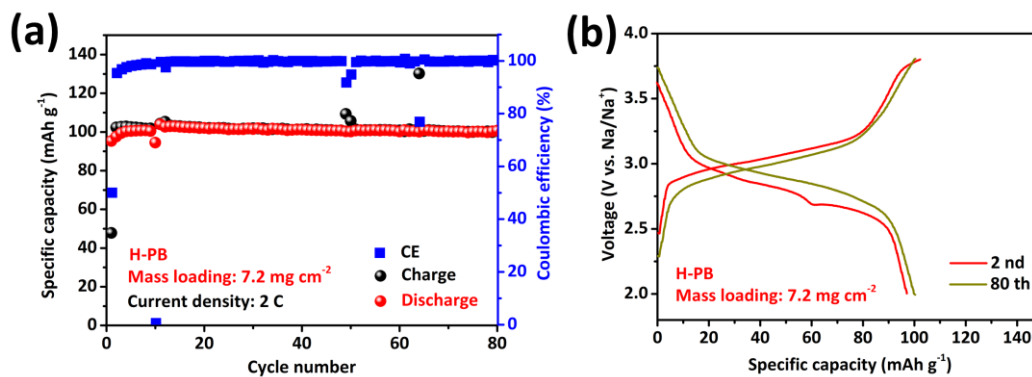

Figure S14. The electrochemical performance of H-PB at high mass loading of 7.2 mg cm^{-2}.
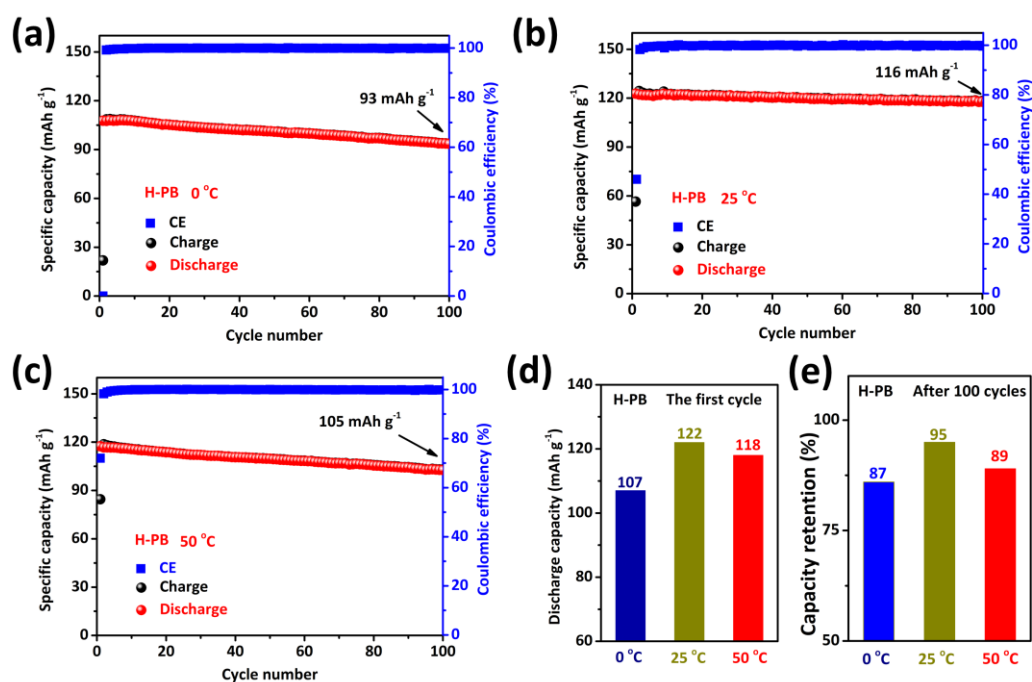

Figure S15. The cycling performance of H-PB at a) 0 $^{\circ}$C, b) 25 $^{\circ}$C and c) 50 $^{\circ}$C. The comparisons of d) first discharge capacities and e) capacity retentions after 100 cycles at varied temperature.

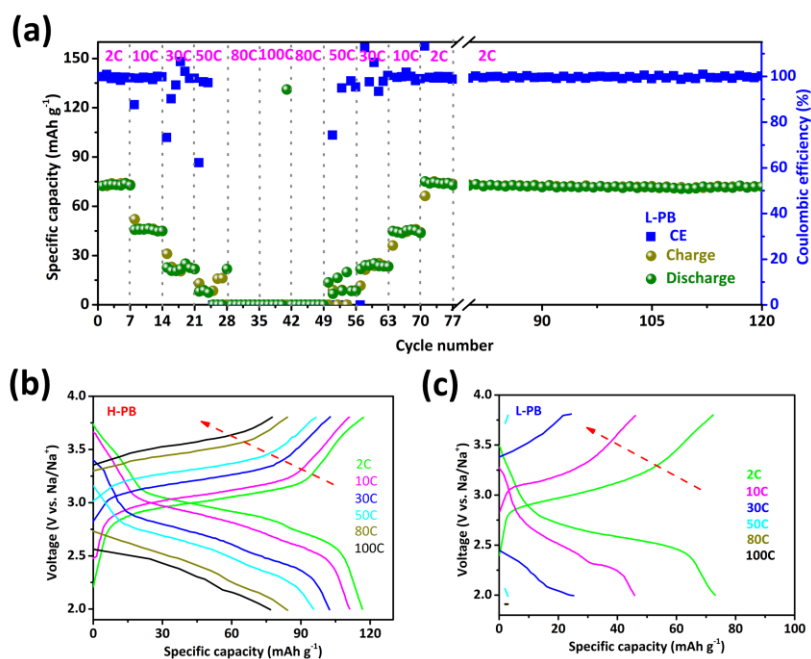**Figure S16.** a) The rate performance of L-PB and corresponding charge and discharge curves of b) H-PB and c) L-PB. The L-PB cannot afford any capacity at high current density due to the sluggish ion diffusion.
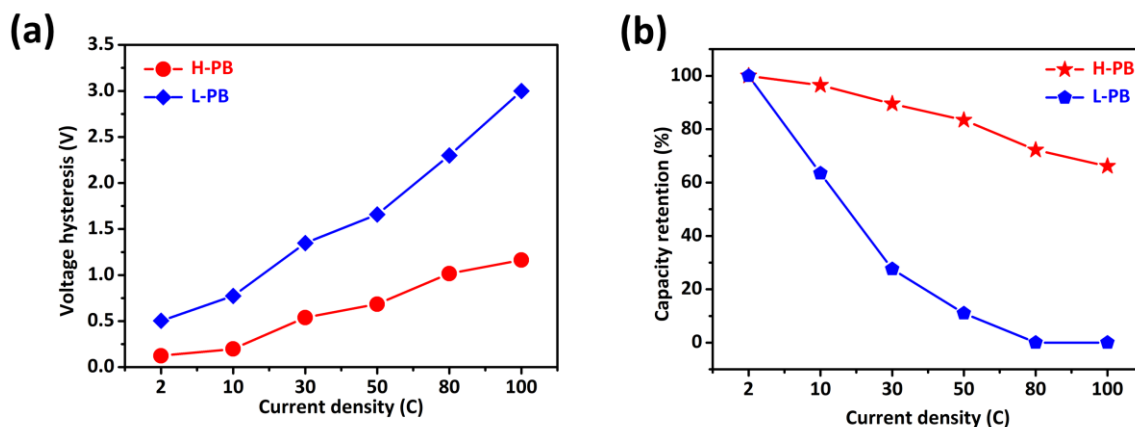

Figure S17. a) The voltage hysteresis and b) capacity retention of two electrodes as a function of the C rate. The voltage hysteresis is calculated from the potential differences at the half charge and discharge states.
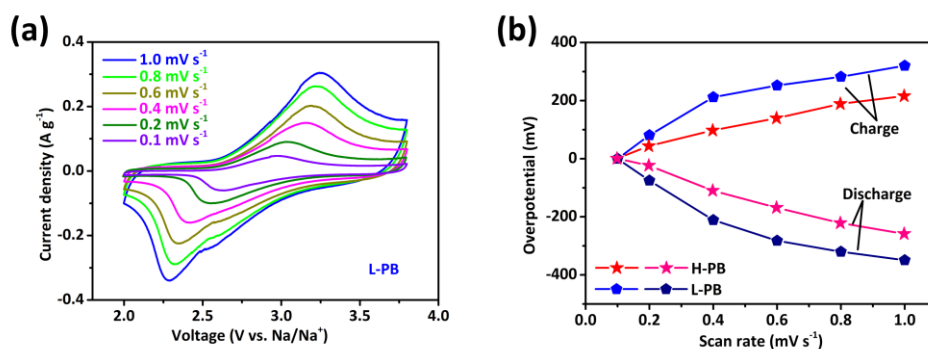
Figure S18. a) The CV results of L-PB at varied scan rates and b) corresponding overpotential variations between H-PB and L-PB.
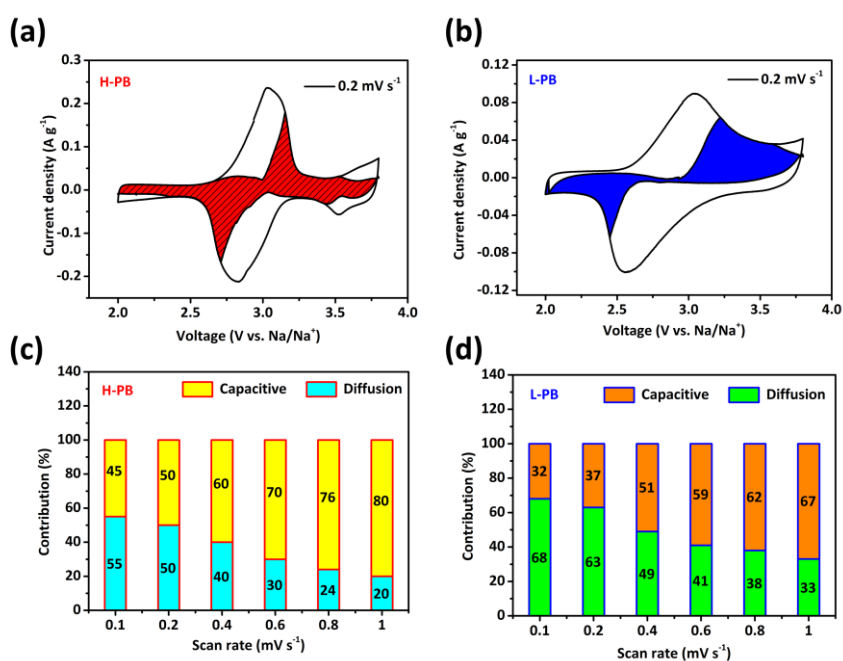
Figure S19. Separation of the capacitive and diffusion currents in a) H-PB and b) L-PB at a scan rate of 0.2 mV s^{-1}. Contribution ratios from the capacitive and diffusion-controlled processes of c) H-PB and d) L-PB at different scan rates.

The detail quantitative characterization of the capacity contribution is based on the following equation[7]:

$$i(V)=K_1v+K_2v^{1/2} \tag{1}$$

The measured current *(i)* at a fixed potential *(V)* can be separated into capacitive effects *(k₁v)*

and diffusion-controlled contributions $(k_2v^{1/2})$.
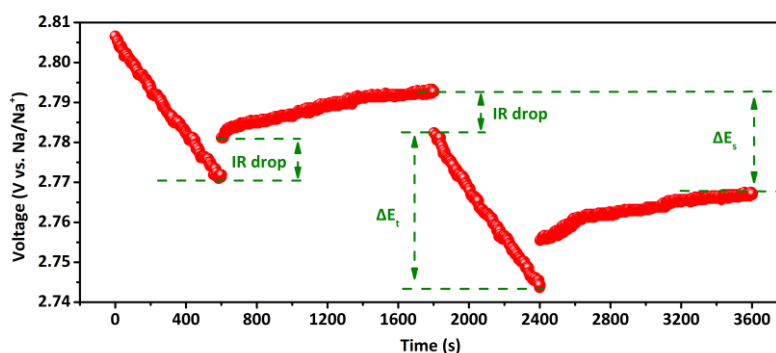
Figure S20. The typical potential response with time in GITT measurement.

The D_{GITT} can be calculated from the potential response to a negligible current pulse. As revealed by the following equation [8]:

$$D_{GITT}=(4/\pi t)(mV_M/MS)^2(\Delta Es/\Delta Et)^2 \tag{2}$$

where t represents each current pulse time, m, V_M, S, and M represent the mass, molar volume, surface area, and molar mass of the active materials, respectively. ΔEs and ΔEt are the voltage differences.

Figure S21. The schematic illusion of fast Na-ion diffusion in H-PB.

Figure S22. EIS spectra of H-PB and L-PB recorded a) at pristine and b) cycled for 20 cycles at 2 C.

The insertion exhibits the calculations based on the Z' values and the reciprocal square root of frequency at the low-frequency region. Notably, two identical semi-spheres can be found at pristine stage for both H-PB and L-PB, indicating the adi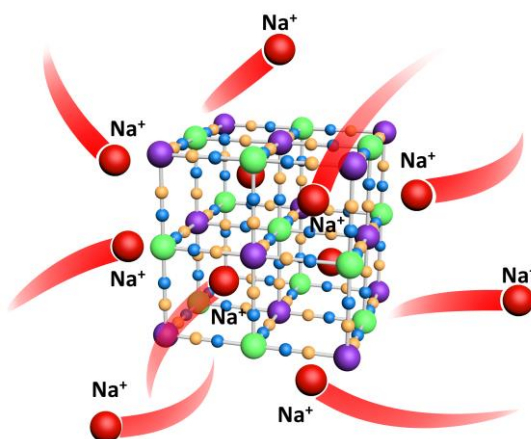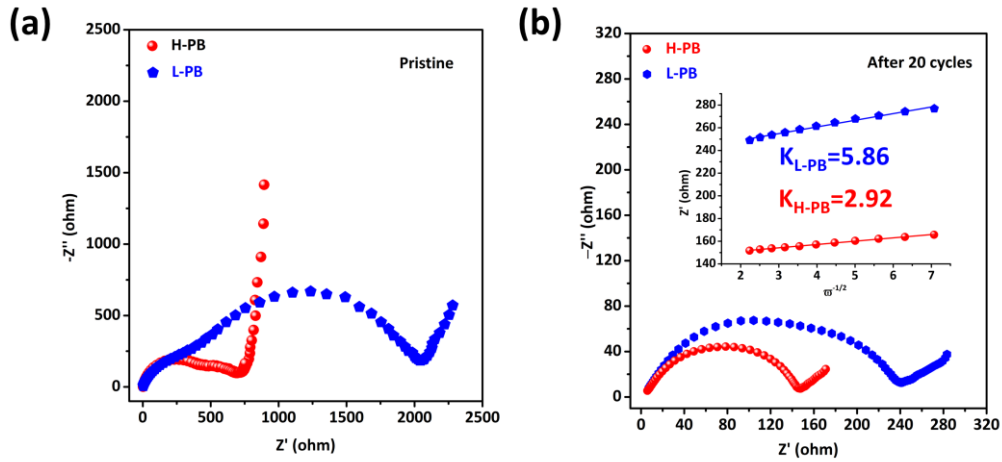on insertion mechanism of Na^+, which means that the charge transfer of Na^+ goes through two interfaces (the two interfaces exist between the outer Helmholtz plane (OHP), the inner Helmholtz plane (IHP) and the electrode). However, after cycles, the charge transfer impedance mainly comes from the impedance between electrolyte and electrode, the impedance at OHP/IHP interface declines quickly due to the easy solvation/desolvation process of Na^+.[9] The Na^+ apparent diffusion coefficient from EIS results (D^{EIS}) are calculated based on the following equations.[4]

$$Z'=R_e + R_{ct} +\delta_w\omega^{-1/2} \tag{3}$$

$$D=0.5(RT/An^2F^2\delta_wC)^2 \tag{4}$$

Where ω is the angular frequency $(2\pi f)$ in the low-frequency region, R_e and R_{ct} are kinetics parameters. Then, the Warburg coefficient δ_w can be obtained from the liner fitting of Z' and $\omega^{-1/2}$ (insert in Figure S18b). According to equation (4), where T denotes the absolute temperature (298 K), R represents the gas constant, F is Faraday constant, A stands for the surface area, n is the number of electrons per molecule and C represents the concentration of Na^+. Apparently,

the Na$^+$ diffusion coefficient has an inverse relationship with the square value of δ_w. Thus, the small slope value of H-PB ($k = 2.92$) compared with L-PB ($k = 5.86$) manifests that the D_{EIS} of H-PB is about an order of magnitude higher than L-PB, which is corresponding to the CV and GITT results.
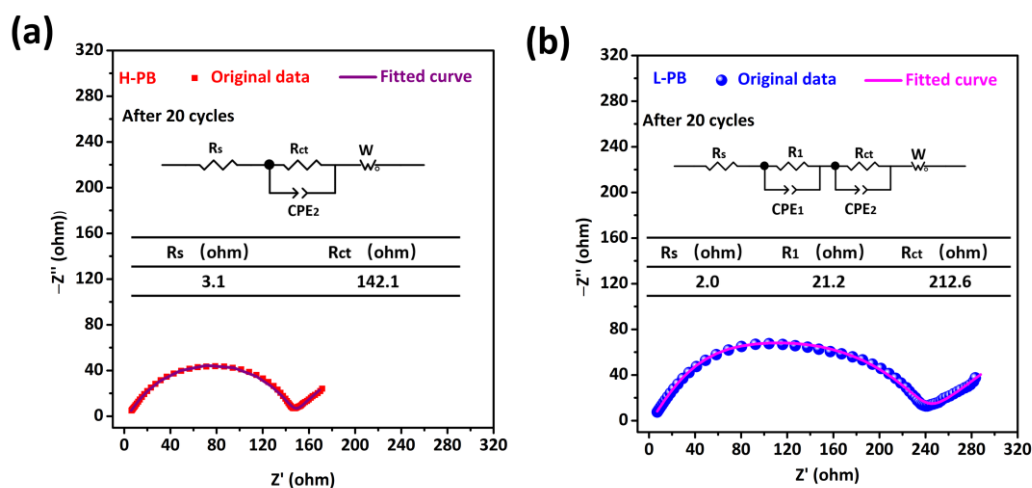
Figure S23. Nyquist plots of a) the cycled H-PB and b) L-PB electrodes in half-cells. Each figure is provided with the equivalent circuit and a table summarizing the value of resistance. Wherein, R_s stands for internal resistance of the cell, R_{ct} stands for charge transfer resistance and R_1 represents the resistance at OHP/IHP interface. The charge transfer resistance of H-PB (142.1Ω) is smaller than L-PB (212.6 Ω), demonstrating excellent electronic conductivity of H-PB. Moreover, an additional resistance of 21.2 Ω exhibited in L-PB within higher frequency region shows the sluggish charge transfer at OHP/IHP interface as explained in Figure S22.
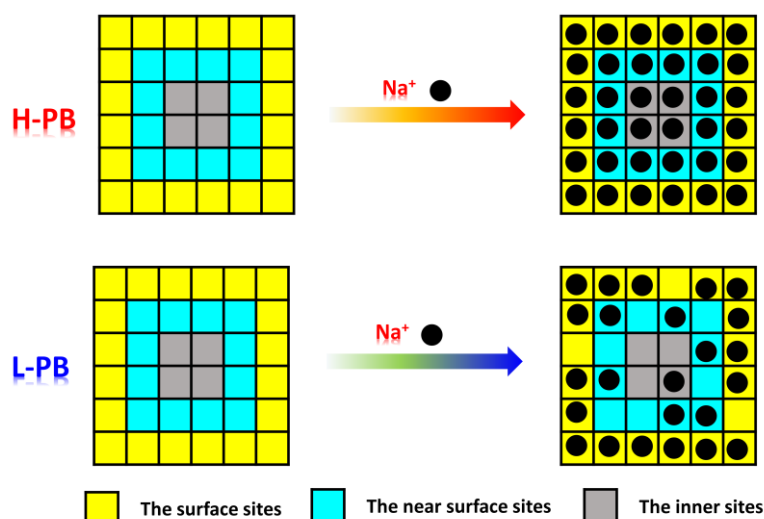
Figure S24. Schematic of outside-in diffusion pathways. Theoretically, the inner sites exhibit lower reaction activity compared with the surface and the near surface sites. Furthermore, the long migration distance for inner sites leads to a typical diffusion-controlled process for Prussian blue. However, the long-range periodicity of crystal lattice in H-PB, ensuring smooth migration channels and realizing high reaction activity of inner sites, leads to significantly enhanced electrochemical kinetics. In addition, the perfect lattice arrangement in H-PB also enables substantial active sites.

Figure S25 a) The typical *in situ* XRD results for H-PB. b) The *ex situ* XRD results for L-PB. There is no phase transition observed in L-PB, which is different from the results concluded for H-PB. The evolution difference is caused by the different amount of Na$^+$ involved in the

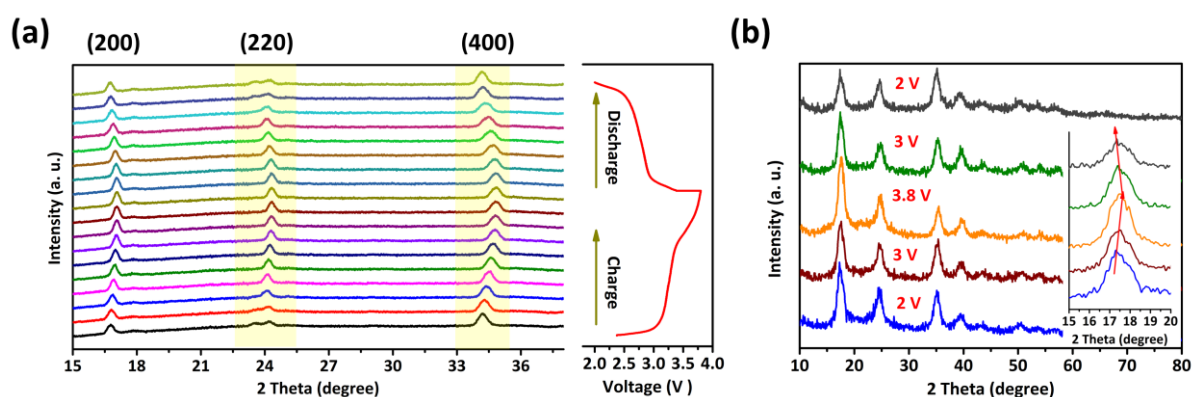electrochemical process. As for H-PB, a phase change from cubic to rhombohedral is happened when discharged to 2.6 V, about 3.2 Na$^+$ (delivering capacity of 95 mAh g^{-1}) inserted into the crystal structure. This evolution is beneficial to release the stress-strain and keep the structure integrate. However, only 2 Na$^+$ (60 mAh g^{-1}) inserted into the L-PB within the electrochemical window, those relatively small parts of Na$^+$ cannot cause extensive inner stress and hence lead to no phase transformation.
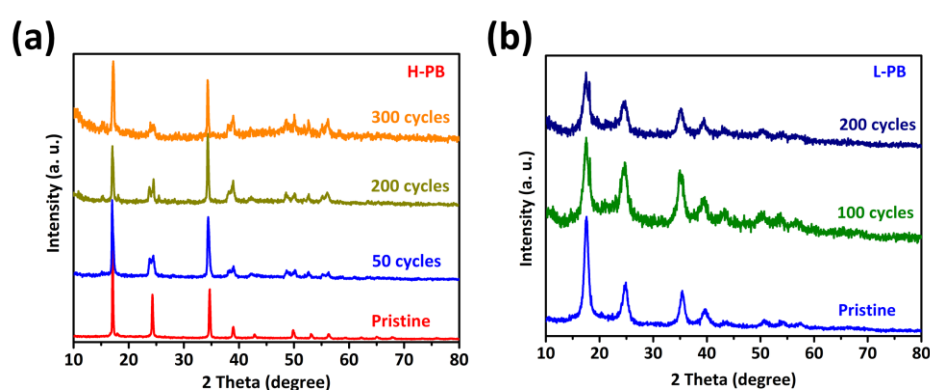

Figure S26. The XRD patterns collected at different cycles for a) H-PB and b) L-PB. The diffraction peaks are well preserved in H-PB. The split peaks around 25, 39 and 50 are attributed to the rhombohedral phase. As a comparison, the peaks become border and weaker in L-PB after several cycles, demonstrating an amorphization process during repeating Na$^+$ insertion and extraction.
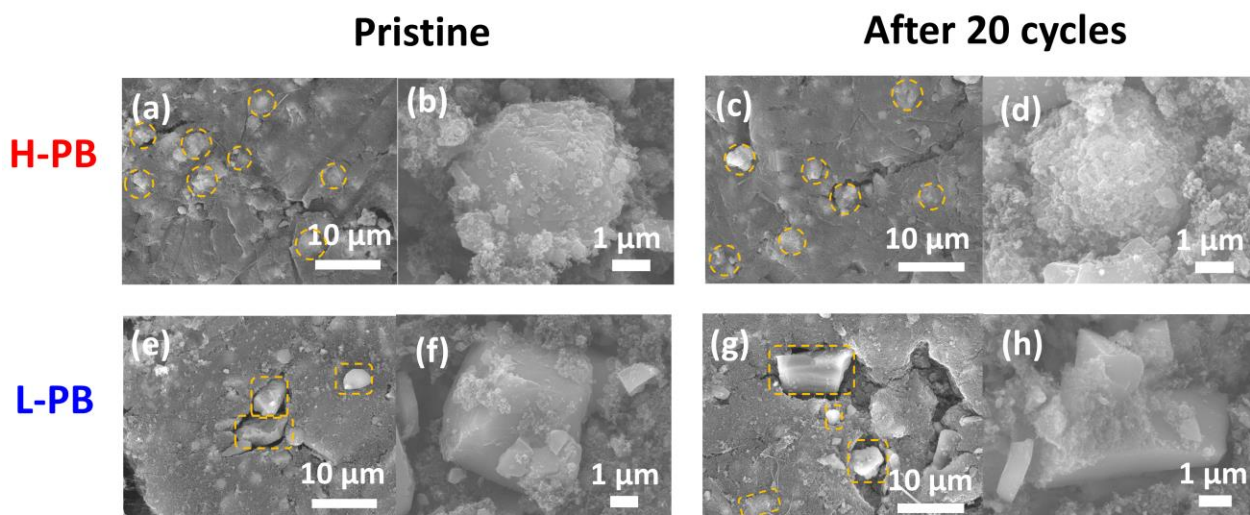
Figure S27. The SEM images for (a, b, c, and d) H-PB and (e, f, g, and h) L-PB at initial stages and after 20 cycles at 2 C.

One can see from the above images that, the H-PB particles are well immersed in the Ketjen black as denoted by yellow circles during cycling, providing excellent electronic conductivity. However, the SEM images of L-PB clearly show gaps between active materials and Ketjen black due to the irregular particle sizes, leading to sluggish charge transfer and inferior electrochemical performance. H-PB and L-PB maintain their initial morphologies and go through negligible size variations after 20 cycles at 2 C. Their intrinsic open-framework structures and large interstitial sites guarantee the morphological integrity, and hence suffer from negligible morphological evolutions during the repeating insertion/deinsertion of Na$^+$ ions.
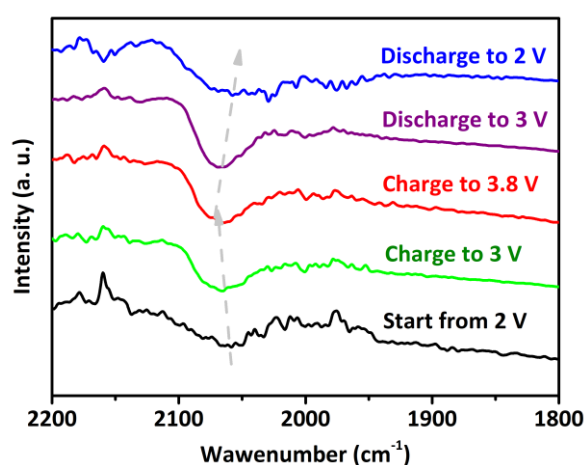
Figure S28. The FT-IR spectra collected at different states for H-PB.
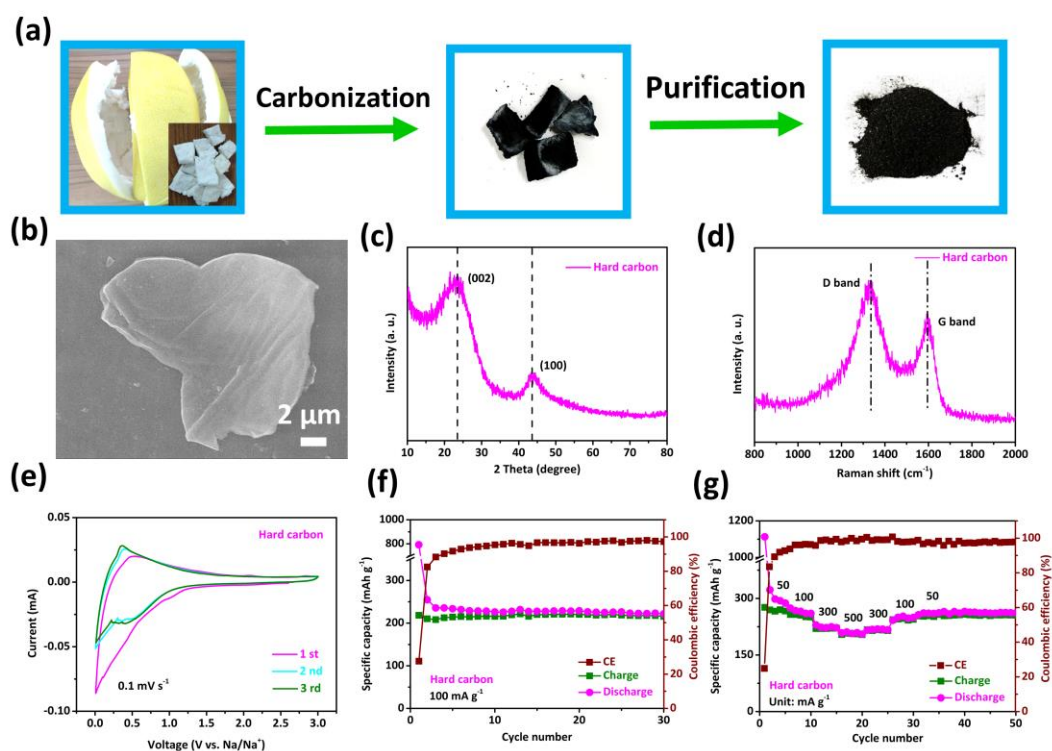
Figure S29. Characterizations for the hard carbon derived from shaddock peels. a) Illustrations for the preparation of hard carbon. b) The typical SEM image, c) XRD pattern and d) Raman spectra of hard carbon. e) CV curves at 0.1 mV s^{-1} within 0.01 to 3 V. f) Cycling stability of hard carbon at 100 mA g^{-1}. g) The rate performance of hard carbon.
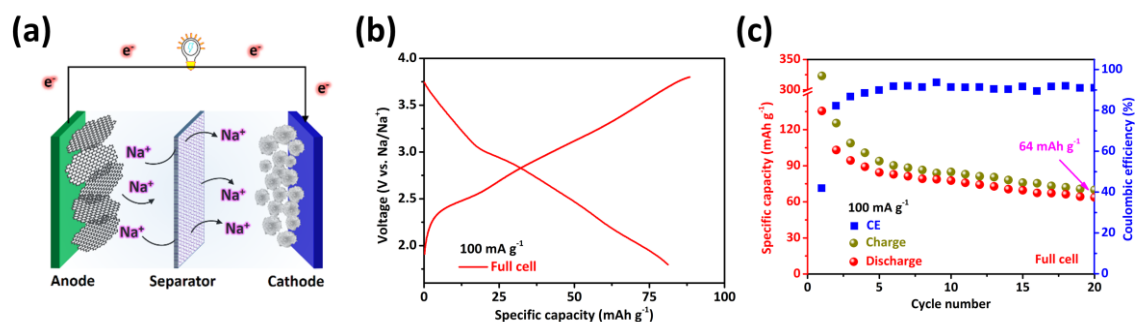
Figure S30. a) The schematic diagram for full cell. b) The typical charge and discharge curves at 100 mA g^{-1}. c) The cycle performance of full cell at 100 mA g^{-1}.

Table S1. The element analysis for H-PB and L-PB.

Sample	Element	Weight %	Atomic %
H-PB	Na	3.97	1.72
	Fe	34.32	6.13
L-PB	Na	1.05	0.46
	Fe	30.29	5.41

The Na contents for two samples were calculated from ICP results as follows:

$$H\text{-}PB: 1.72/6.13\times7=1.96 \tag{5}$$

$$L\text{-}PB: 0.46/5.41\times7=0.60 \tag{6}$$

Table S2. The structural comparison between H-PB and L-PB based on the Rietveld-refinements

Samples	Chemical formula	Crystal system	Lattice parameter (Å)	Cell volume (Å^3)
H-PB	$Na_2Fe_4[Fe(CN)_6]_3$	Cubic	a=b=c=10.36 α=β=γ=90°	1111.93
L-PB	$Na_{0.6}Fe_4[Fe(CN)_6]_3$	Cubic	a=b=c=10.04 α=β=γ=90°	1012.05

H-PB and L-PB represent the same crystal system of cubic lattice, whereas H-PB exhibits larger cell volume due to the slightly expanded lattice parameter.

Table S3. The detailed fitting parameters of H-PB and L-PB

Sample	Structure	δ (mm s^{-1})	Qs (mm s^{-1})	Area ratio (%)
H-PB	LS-Fe^{2+}	-0.087	0.076	36.3
	HS-Fe^{2+}	0.863	0.896	20.0
	HS-Fe^{3+}	0.370	0.4800	31.2
	HS-Fe^{2+}	0.600	0.200	12.5
L-PB	LS-Fe^{2+}	-0.118	0.131	34.5
	HS-Fe^{3+}	0.374	0.497	65.5

Table S4. The sodium storage performance of as synthesized Prussian blue and its Analogues.

Samples	Cycle life (Capacity retention）	Rate capability (capacity mAh g^{-1})	Refs.
H-PB	**2,000 (62%)**	**100 C (78 mAh g^{-1})** **50 C (95 mAh g^{-1})**	**This work**

$Fe_4[Fe(CN)_6]_3$	50 (86%)	0.1 A g^{-1} (90 mAh g^{-1})	1
$Na_{1.58}Fe[Fe(CN)_6]_{0.92}$	800 (90%)	10 C (76 mAh g^{-1})	10
$Na_{2-\delta}MnHCF$	500 (75%)	20 C (120 mAh g^{-1})	11
NMFHFC	200 (80.2%)	20 C (21 mAh g^{-1})	12
HQ-NaFe	150 (100%)	0.6 A g^{-1} (80 mAh g^{-1})	13
$FeFe(CN)_6$	500 (87%)	20 C (78 mA h g^{-1})	14
NaK-MnHCF@3DNC	100 (68%)	0.5 A g^{-1} (110 mAh g^{-1})	15
$NaFe_2(CN)_6$	3000 (61%)	50 C (46.0 mAh g^{-1})	16
$Na_{0.99}Mn_{0.37}Fe_{0.63}[Fe(CN)_6]_{0.96}$	300 (100%)	20 C (90.5 mAh g^{-1})	17
HQ-MnCoNi-PB	500 (81.1%)	9 C (70 mAh g -1)	18

References

(1) Sun, H.; Sun, H.; Wang, W.; Jiao, H.; Jiao, S. $Fe_4[Fe(CN)_6]_3$: a Cathode Material for Sodium-Ion Batteries. *RSC Adv.* **2014,** *4*, 42991-42995.

(2) Sun, N.; Liu, H.; Xu, B. Facile Synthesis of High Performance Hard Carbon Anode Materials for Sodium Ion Batteries. *J. Mater. Chem. A* **2015,** *3*, 20560-20566.

(3) Toby, B. H. EXPGUI, a Graphical User Interface for GSAS. *J. Appl. Crystallogr.* **2001,** *34*, 210-213.

(4) Ren, W.; Qin, M.; Zhu, Z.; Yan, M.; Li, Q.; Zhang, L.; Liu, D.; Mai, L. Activation of Sodium Storage Sites in Prussian Blue Analogues via Surface Etching. *Nano Lett.* **2017,** *17*, 4713-4718.

(5) Marco, J. F.; Gancedo, J. R.; Gracia, M.; Gautier, J. L.; Rios, E.; Berry, F. Characterization of the Nickel Cobaltite, $NiCo_2O_4$, Prepared by Several Methods: an XRD, XANES, EXAFS, and XPS Study. *J. Solid State Chem.* **2000,** *153*, 74-81.

(6) Byon, H. R.; Gallant, B. M.; Lee, S. W.; Shaohorn, Y. Role of Oxygen Functional Groups

in Carbon Nanotube/Graphene Freestanding Electrodes for High Performance Lithium Batteries. *Adv. Funct. Mater.* **2013,** *23*, 1037-1045.

(7) Chen, C.; Wen, Y.; Hu, X.; Ji, X.; Yan, M.; Mai, L.; Hu, P.; Shan, B.; Huang, Y. Na+ Intercalation Pseudocapacitance in Graphene-Coupled Titanium Oxide Enabling Ultra-Fast Sodium Storage and Long-Term Cycling. *Nat. Commun.* **2015,** *6*, 6929.

(8) Wang, W.; Gang, Y.; Hu, Z.; Yan, Z.; Li, W.; Li, Y.; Gu, Q.-F.; Wang, Z.; Chou, S.-L.; Liu, H.-K.; Dou, S.-X. Reversible Structural Evolution of Sodium-Rich Rhombohedral Prussian Blue for Sodium-Ion Batteries. *Nat. Commun.* **2020,** *11*, 980.

(9) Fu, H.; Liu, C.; Zhang, C.; Ma, W.; Wang, K.; Li, Z.; Lu, X.; Cao, G. Enhanced Storage of Sodium Ions in Prussian Blue Cathode Material Through Nickel Doping. *J. Mater. Chem. A* **2017,** *5*, 9604-9610.

(10) Tang, X.; Liu, H.; Su, D.; Notten, P. H. L.; Wang, G. Hierarchical Sodium-Rich Prussian Blue Hollow Nanospheres as High-Performance Cathode for Sodium-Ion Batteries. *Nano Res.* **2018,** *11*, 3979-3990.

(11) Song, J.; Wang, L.; Lu, Y.; Liu, J.; Guo, B.; Xiao, P.; Lee, J. J.; Yang, X.; Henkelman, G.; Goodenough, J. B. Removal of Interstitial H_2O in Hexacyanometallates for a Superior Cathode of a Sodium-Ion Battery. *J. Am. Chem. Soc.* **2015,** *137*, 2658-2664.

(12) Li, W.; Han, C.; Wang, W.; Xia, Q.; Chou, S.; Gu, Q.; Johannessen, B.; Liu, H.; Dou, S. Stress Distortion Restraint to Boost the Sodium Ion storage Performance of a Novel Binary Hexacyanoferrate. *Adv. Energy Mater.* **2019,** *10*, 1903006.

(13) You, Y.; Wu, X.; Yin, Y.; Guo, Y. High-Quality Prussian Blue Crystals as Superior Cathode Materials for Room-Temperature Sodium-Ion Batteries. *Energy Environ. Sci.* **2014,** *7*, 1643-1647.

(14) Wu, X.; Deng, W.; Qian, J.; Cao, Y.; Ai, X.; Yang, H. Single-Crystal FeFe(CN)6 Nanoparticles: a High Capacity and High Rate Cathode for Na-Ion Batteries. *J. Mater. Chem. A* **2013,** *1*, 10130-10134.

(15) Mao, Y.; Chen, Y.; Qin, J.; Shi, C.; Liu, E.; Zhao, N. Capacitance Controlled, Hierarchical Porous 3D Ultra-Thin Carbon Networks Reinforced Prussian Blue for High Performance Na-Ion Battery Cathode. *Nano Energy* **2019,** *58*, 192-201.

(16) Li, W.; Han, C.; Xia, Q.; Zhang, K.; Chou, S.; Kang, Y. M.; Wang, J.; Liu, H. K.; Dou, S. X. Remarkable Enhancement in Sodium-Ion Kinetics of $NaFe_2(CN)_6$ by Chemical Bonding with Graphene. *Small Methods* **2018,** *2*, 1700346.

(17) Feng, F.; Chen, S. L.; Liao, X. Z.; Ma, Z. F. Hierarchical Hollow Prussian Blue Rods Synthesized via Self-Sacrifice Template as Cathode for High Performance Sodium Ion Battery. *Small Methods* **2019,** *3*, 1800259.

(18) Xie, B.; Zuo, P.; Wang, L.; Wang, J.; Huo, H.; He, M.; Shu, J.; Li, H.; Lou, S.; Yin, G. Achieving Long-Life Prussian Blue Analogue Cathode for Na-Ion Batteries via Triple-Cation Lattice Substitution and Coordinated Water Capture. *Nano Energy* **2019,** *61*, 201-210.